crystals

MDPI

Article

Hydrothermal Synthesis, Characterization and Exploration of Photocatalytic Activities of Polyoxometalate: Ni-$CoWO_4$ Nanoparticles

Fahad A. Alharthi *,†, Hamdah S. Alanazi †, Amjad Abdullah Alsyahi and Naushad Ahmad

Department of Chemistry, College of Science, King Saud University, Riyadh 11451, Saudi Arabia; hsenzi@ksu.edu.sa (H.S.A.); A.Alsyahi@hotmail.com (A.A.A.); anaushad@ksu.edu.sa (N.A.)

* Correspondence: fharthi@ksu.edu.sa

† These authors are contributed equally to this work.

Abstract: This study demonstrated the hydrothermal synthesis of bimetallic nickel-cobalt tungstate nanostructures, Ni-$CoWO_4$ (NCW-NPs), and their phase structure, morphology, porosity, and optical properties were examined using X-ray Diffraction (XRD), Fourier-transform infrared spectroscopy (FT-IR), Scanning electron microscopy- energy dispersive X-ray spectroscopy (SEM-EDS), high resolution Transmission electron microscopy (HR-TEM), Brunauer-Emmett-Teller (BET) and Raman instruments. It was found that as-calcined NCW-NPs have a monoclinic phase with crystal size ~50–60 nm and is mesoporous. It possessed smooth, spherical, and cubic shape microstructures with defined fringe distance (~0.342 nm). The photocatalytic degradation of methylene blue (MB) and rose bengal (RB) dye in the presence of NCW-NPs was evaluated, and about 49.85% of MB in 150 min and 92.28% of RB in 90 min degraded under visible light. In addition, based on the scavenger's study, the mechanism for photocatalytic reactions is proposed.

Keywords: bimetallic tungstate; Raman spectroscopy; methylene blue; rose bengal; photocatalytic activity; scavenger

Citation: Alharthi, F.A.; Alanazi, H.S.; Alsyahi, A.A.; Ahmad, N. Hydrothermal Synthesis, Characterization and Exploration of Photocatalytic Activities of Polyoxometalate: Ni-$CoWO_4$ Nanoparticles. *Crystals* **2021**, *11*, 456. https://doi.org/10.3390/cryst11050456

Academic Editors: Ewa Wierzbicka, Karolina Syrek and Alessandro Vergara

Received: 31 December 2020
Accepted: 19 April 2021
Published: 21 April 2021

1. Introduction

Among the various catalytic reaction, photocatalysis (activation of catalyst by light absorption of suitable wavelength/bandgap energy) has drawn much attention because photo-irradiation of the catalyst not only increases the reaction process, but also reduces the initiation path and activation energy without its involvement as reactants and products [1]. The photocatalysis process is a useful, advantageous, and economical low-cost process as well as a sustainable solution to eliminate various toxic chemicals from the environment and water such as removal/mineralization of dyestuffs and clean energy production including hydrogen fuel by water splitting [1–3]. In the photocatalytic process, photocatalysts generate active species according to their bandgap ranges in the presence of a light source (ultraviolet/visible light), which aids the mineralization of dyes into CO_2 and H_2O using an advanced oxidation route.

Various semiconductor photocatalysts have been developed by research groups to keep zones of the Earth and atmosphere clean: terrestrial (forest, grassland, desert) and aquatic (biotic and abiotic) ecosystems [1,3–5]. In this study, our research group reported semiconducting photocatalytic materials, which make different dyes active [6–9]. For the complete elimination of dye contaminants, researchers have mainly focused on developing special features of semiconductors for better degradation performance. The best-fitting parameters for the dye degradation are that the photocatalyst must have a low recombination rate of charge carriers (electron-hole pairs), extended wavelength/narrow bandgaps, high rate of electron transfer, and large facility for the photocatalytic reaction/chemisorption on its surface. These features can be achieved using various strategies such as morphology

alteration, doping, compositing, and the coupling of inorganic and organic precursors (e.g., carbon nitrides, reduced graphene, noble metals, and nonmetals) in semiconductors to achieve a state of capturing the visible-light region of solar spectrum [1–11]. In this study, compared to other modification methods, the combination of two or more semiconductors with a different bandgap and a certain amount of impurity ion doping (e.g., Zn, Cu, Ni, Co and Mn) in host materials (hybrids and heterojunctions) was a better choice and opens a new window for conventional and advanced nanostructures. This new nanostructure can alter the selected properties (morphology, surface area, bandgap or optical properties) for multifunctional catalysis in various fields such as electronics, magnetism, optics, catalysis, electrochemistry, etc. [10–12]. Well-known TiO_2 photocatalysts are used for the degradation of dyes in UV light, but insensitivity to visible light and low quantum yield limits its application [13,14]. However, to overcome these limitations, doping/incorporation with cations, anions, and carbons increases their photocatalytic activity [5,11,12]. Recently, several groups have directed their research toward this area. For example, Chowdhury et al. prepared $SnWO_4$ nanoparticles and used them for the photodegradation of Rhodamine B and Brilliant green. He degraded less than 50% of the dyes, but on the addition of BiOBr by the coprecipitation method, the obtained BiOBr-$SnWO_4$ heterojunction nanocomposites showed better photocatalytic performance than the bare $SnWO_4$ [15]. Similar effects were observed by the Yangjeh group [16].

However, searching for new materials with the above features is essential in fabricating outstanding visible-light sensitive conducting materials, specifically n-type semiconductors. Currently, from a technological viewpoint, tungsten oxides are important photochromic semiconductors and potential photocatalytic materials because of their intriguing properties such as good conductivity, electrical, thermal, and optical activeness in the visible region [15–19]. Narrow bandgap tungstates are more efficient semiconductors for photocatalytic performance compared to wide band-gap materials because they adsorb a larger fraction of solar light. Huang et al. developed a $Zn_{1-x}Ni_xWO_4$ ($0 \leq x \leq 1$) solid solution using hydrothermal annealing and observed that the optical band-gap energy red-shifted from 2.8 to 1.63 eV for indirect transition and 3.56 to 2.77 eV for direct transition with the doping Ni^{2+} ion [20]. Considering these properties, tungstates are used to fabricate various devices such as sensors, detectors, optical fibers/displays, luminance lamps, and energy storage devices including supercapacitors and batteries. Zhang and Xu et al. [21,22] successfully prepared a $CoWO_4/Co_3O_4$ and Co_3O_4@$CoWO_4$/rGO heterostructure, which displayed excellent electrochemical performance as electrode materials.

To improve the photolytic efficiency of tungstate, various methods have been used to fabricate nanosize materials: coprecipitation, sol-gel process, physical vapor deposition, chemical vapor deposition, electrochemical deposition, spray pyrolysis, vacuum evaporation, dip-coating, polymer-assisted deposition and hydrothermal process as well as traditional microwave irradiation [1,17–23]. The preparation of tungstates depends on physical-chemical properties and catalytic activities toward a specific application. Among the methods mentioned, the hydrothermal approach is one of the most promising routes that can be controlled through an appropriate choice of reaction parameters such as temperature, time, pH, mineralizer, and surfactant because of its high efficiency, simplicity, and low cost compared to other conventional methods [19–21,24]. The merits of hydrothermally synthesized tungstate semiconductors are large surface area, reproducibility, nanosized selective morphology, and ample possibilities to easily tune the bandgap to fit a required application. Various methods have been employed to fabricate $CoWO_4$: coprecipitation, solid-state, sol-gel, aqueous solution growth, polymerized complex matrix, molten salt, self-propagating combustion, hydrothermal, etc. [21,22,25,26]. Among them, the hydrothermal method is the most effective way to dope other transition M^{2+} ions into the lattice of $CoWO_4$ for electron transfer, depending on their edge potentials. Doping of Ni^{2+} in various oxide systems (Al_2O_3, CeO_2, ZrO_2) shows promising performances, especially in industrial methane reforming reactions, supercapacitors, gas sensors, and optics [27–30]. For the photocatalytic process, Ni^{2+} is a suitable doping agent because of its optical band-gap energy

[3.6–4.0 eV] [31] and has a controlling influence on the electronic and optical properties of host nanostructures. Considering the above facts, we report the synthesis of bimetallic Ni-$CoWO_4$ nanoparticles using the hydrothermal method and explorations of its crystal structure, morphological, optical, and surface properties using sophisticated techniques. Photocatalytic activity against rose bengal and methylene blue dyes are looked at in detail.

2. Experimental

2.1. Synthesis of Ni-$CoWO_4$ (NCW-NPs)

All chemicals and reagents used were of analytical grade and were procured from the Aldrich chemical corporation, USA, and used without any further purification. In a hydrothermal procedure for the fabrication of NCW-NPs, 1 mmol of $Ni(NO_3)_2.6H_2O$ and $Co(NO_3)_2.6H_2O$ was dissolved in 50 mL DI water and heated at 50 °C for 30 min without adding any surfactants and additives. To this mixed solution, 4 mmol $Na_2WO_4.2H_2O$ was added slowly and then heated for 30 min until a suspension was achieved. The resulting suspension of the precursors was supplemented in 100 mL capacity of Teflon-lined stainless-steel autoclave and heated at 150 °C for 6 h. The cooled product was centrifuged and washed with water and ethanol three times. Finally, the oven-dried amorphous product was air calcined at 600 °C with a heating rate of 10 °C/min for 5 h.

2.2. Characterization

The crystallographic structure of fine powders was investigated via X-ray diffraction analysis in the range of 10°–80° (2θ angle rotation) using an X-ray diffractometer (Shimadzu 7000S, Shimadzu Analytical, Kyoto, Japan) equipped with CuK_α radiation (λ = 0.154 nm). The infrared spectrum was recorded using a FTIR spectrometer (3000 Hyperion Microscope with Vertex 80 FTIR System; Bruker, Karlsruhe, Germany). The Raman spectrum was conducted with the use of a Renishaw micro-Raman spectrometer (RE-04) equipped with a solid-state laser diode-pumped at 514 nm. The morphological and elemental analyses were examined using scanning electron microscopy-energy dispersive x-ray spectroscopy (SEM-Hitachi S3400, Sydney, Australia; operating voltage = 10 kV) Additionally, to obtain more information about the microstructure of the material, transmission electron microscopy (TEM) was performed on an FEI Tecnai G2, F30 electron microscope with an operating voltage of 200 kV and resolution of 2.0 Å. The average crystallinity of the material was studied using the selected area electron diffraction (SAED) technique. The surface area and pore volume of the material were determined by nitrogen adsorption-desorption isotherm measured at 77 K on a BET surface analyzer (Micromeritics ASAP 2010, Norcross, GA, USA). Before each measurement, the sample was degassed at 200 °C under vacuum for 2 h before N_2 adsorption. Surface area and pore volumes were calculated using the Brunauer-Emmet-Teller (BET) equation and BJH methods, respectively.

2.3. Photocatalytic Measurement

Cationic (MB) and anionic (RB) dyes were used to evaluate the photocatalytic reactivity of the as-calcined NCW-NPs in response to visible light. The experiments were conducted as follows: 50 mg catalyst was placed in 5 ppm aqueous solution of dyes in a 100 mL beaker. Before illumination, the suspension was stirred in the dark for 1 h to ensure the establishment of an absorption–desorption equilibrium of dyes on the catalyst surface. Subsequently, the suspension was irradiated under a 300 W Xe lamp with a filter (λ > 420 nm) as a cutoff, about 10 cm away from the beaker. At given intervals, 2 mL of the suspension was extracted and centrifuged to separate the NPs. UV–Vis absorption spectra of the supernatant were then measured using a spectrophotometer (Jasco-770 Spectrometer). The characteristic absorptions of RB (λ = 547 nm) and MB (λ = 663 nm) were chosen as the controlled parameter, and the photocatalytic degradation were performed at the

range of 200–800 nm for 90 and 150 min for the RB and MB, respectively. The degradation efficiency was calculated using the following formula:

$$\text{Degradation efficiency } (\%) = \frac{A_o - A_t}{A_o} \times 100\% \quad (1)$$

where A_o and A_t symbolize the initial absorbance and absorbance at time t of the chosen dyes, respectively. The simplified pseudo-first-order kinetic model of Langmuir–Hinshewood equation was used to estimate the rate constant for the degradation, in other words,

$$ln\frac{A_t}{A_o} = -kt \quad (2)$$

where t is degradation time (min) and k is the rate constant (min^{-1}). According to Equation (2), the rate constant k is the slope of fitting curves, when plotting $ln(A_o/A_t)$ vs. t. In addition, trapping experiments were performed for the determination of the photocatalytic reaction mechanism using various scavengers: tertiary butyl alcohol (TBA), disodium ethylenediamine tetra-acetic acid (EDTA), ascorbic acid (AA), and dichromate ($K_2Cr_2O_7$). The method is similar to the above-mentioned photocatalytic activity test with the addition of 10 mmol/L of trapping agents. The scavengers were added before the addition of the catalyst into the RB dye solution.

3. Results and Discussion

3.1. X-ray Diffraction

X-ray diffraction patterns of the as-synthesized and calcined powder along with their Rietveld refinements are shown in Figure 1a–c. Figure 1a shows the XRD pattern of both samples. We observed that the as-synthesized diffraction pattern showed several peaks and reflected the presence of the mixed-phase, $CoWO_4$, and Co_3O_4 but no existence of NiO (Figure 1b). However, when it was calcined at 600 °C, peaks were suppressed and showed sharp crystalline planes in the as-calcined sample (Figure 1c). The intensity of nanoparticles increased after calcination. From this pattern, it can be indexed to the monoclinic phase with space group P2/a of the fabricated Ni-$CoWO_4$, consistent with the JCPDS card no. 015-0867 [32]. The intensity of the peaks assigned to the phases demonstrates the dimensions (FWHM) of the Ni-$CoWO_4$ nanostructures. Table 1 shows the lattice parameters and crystallite size of both samples. The crystallite sizes of both samples were calculated using the Debye–Scherrer equation [33].

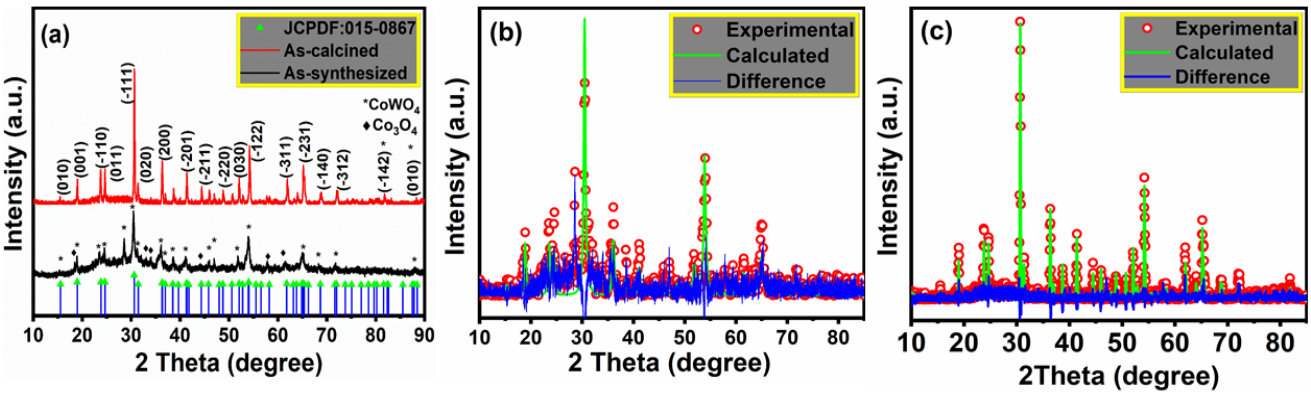

Figure 1. (**a**) X-ray powder diffraction patterns with JCPDF card and Rietveld refinement profile of the (**b**) as-synthesized and (**c**) calcined Ni-$CoWO_4$ NPs.

Table 1. Lattice parameters of the fabricated Ni-$CoWO_4$ NPs.

Powder	a (Å)	b (Å)	c (Å)	Phase	D (nm)
As-calcined	4.634	5.670	4.923	Monoclinic	22.538
As-synthesized	4.641	5.689	4.959	Monoclinic	43.185

3.2. FT-IR Analysis

FTIR spectroscopic analysis was performed to examine the chemical bonds and functional groups in the materials. The spectrum of calcined NCW-NPs is depicted in Figure 2. A wide and shallow peak observed in the range of 3000–3420 cm^{-1} can be ascribed to the O–H stretching mode of adsorbed water molecules. The peak obtained at 2310 cm^{-1} was related to the CO_2, whereas an intense peak was observed at 1632 cm^{-1} for the H–O–H molecule. The characteristic IR bands in the low-frequency region between 400–1000 cm^{-1} can be related to the Co–O, Ni–O, W–, and W–O–W bridges (Figure 2 inset). The two bands at 824 cm^{-1} and 659 cm^{-1} were recognized as the O–W–O vibration and W–O stretching mode, whereas the absorption peaks at 525 cm^{-1} and 461 cm^{-1} are related to the vibrational mode of the Co–O and Ni–O bonds, respectively [34–37].

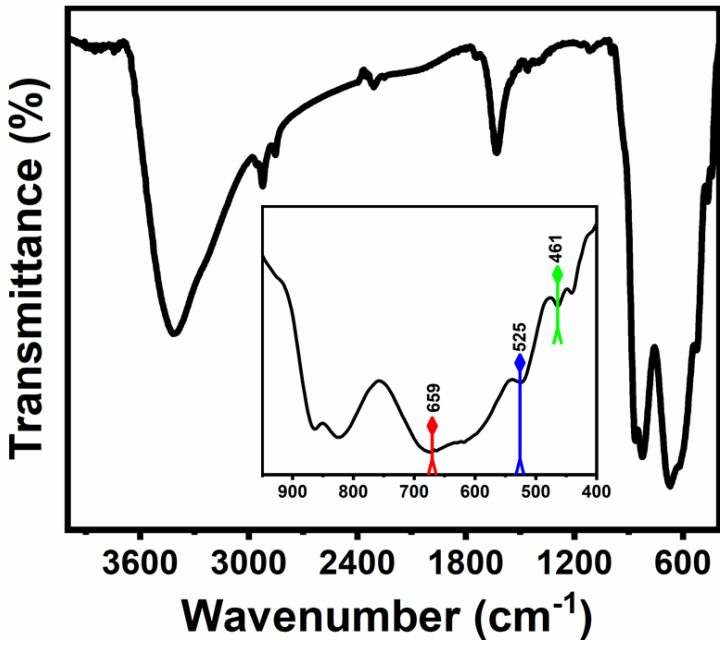

Figure 2. FT-IR spectrum of the calcined Ni-$CoWO_4$ NPs.

3.3. Raman Spectroscopy

The calcined nanocrystal was characterized using a nondestructive Raman spectroscopy technique to understand the structural defects. Figure 3 shows the Raman spectrum for the fabricated NCW-NPs. The peaks appeared at 102, 142, 208, 290, 350, 416, 537, 694, and 889 cm^{-1} positions corresponding to the spectrum of bimetallic Ni-$CoWO_4$ nanoparticles. The sharp band at 889 cm^{-1} was allocated to the symmetric mode of terminal W=O. The weak bands at 694 cm^{-1} and 537 cm^{-1} were antisymmetric and symmetric modes of O–W–O bridgings associated with tungstate anions. In-plane deformation and rotational mode of W–O bonds were observed at 416 cm^{-1} and 350 cm^{-1}, respectively. The band at 102 cm^{-1} and 142 cm^{-1} was attributed to the lattice vibration. Weak bands at 208 and 290 cm^{-1} were associated with Ni–O and Co–O stretching, respectively. All Raman bands were in agreement with the reported results [31,38,39]. Two more band signals are shown at a higher wavenumber (Figure 3 inset) because of the presence of the hydroxyl

group, agreeing with the IR results [39]. Thus, the fabricated bimetallic structured material exhibited a monoclinic phase and correlated with the X-ray diffraction pattern.

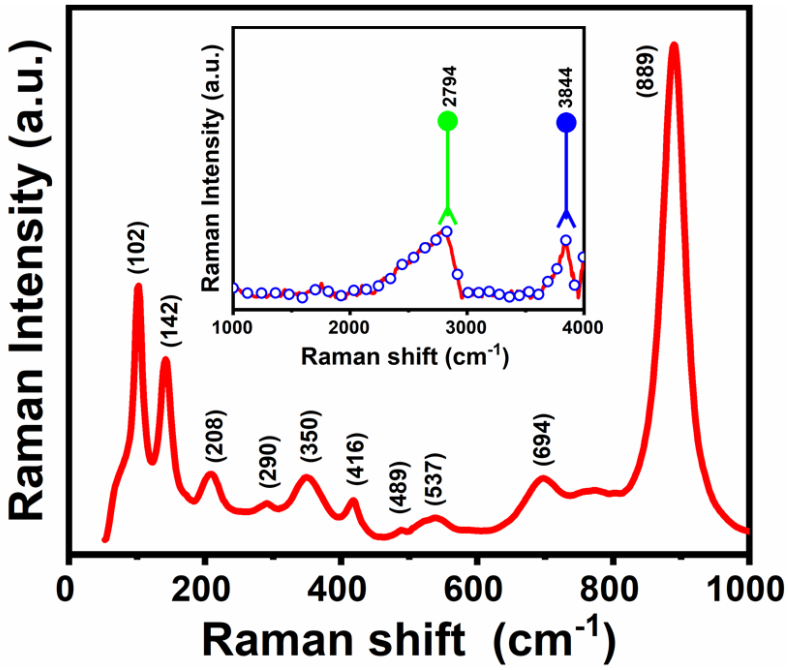

Figure 3. Raman spectrum of the calcined Ni-$CoWO_4$ NPs.

3.4. Morphological Analysis

Figure 4 represents the low and high magnification images of the fabricated NCW-NPs. From the low magnification image (Figure 4a), it appears that nanoparticles formed a cluster of spherical and cauliflower-like morphology with the combination of several nano- and microparticles. The NCW-NP structures were analyzed with a magnified image (Figure 4b). From the image, it was observed that the nanoparticles were closely packed, and the estimated diameter of each cluster of spherical NPs ranged from 10 to 12 µm. The elemental analysis of nanoparticles was observed via EDX spectroscopy and is shown in Figure 4c. It can be seen that carbon, cobalt, nickel, tungsten, and oxygen peaks appeared in the EDX spectrum. A small peak of C was also seen in the spectrum, which relates to carbon tapes used in holding the sample during the EDX analysis. No impurity peak was detected in the EDX spectrum, their atomic ratios of carbon (11.84%), oxygen (65.40%), cobalt (5.78%), nickel (6.23%), and tungsten (10.75%) confirm that the synthesized nanoparticles were bimetallic $NiCoWO_4$ in nature.

The morphology of the NCW-NPs with their crystalline character was analyzed using TEM and the SAED facility. Figure 5a,b shows the low and high magnification TEM images, which represent several spherical and monoclinic/cubic shaped NPs with smooth surfaces arranged on the whole surfaces, indicating that the nanoparticles were not in aggregated forms. This is because during sample preparation for TEM analysis, it was first sonicated for 10 min, appearing non-aggregated. By TEM analysis, it was confirmed that during sonication, the particle well separated because it showed no broken or rough surfaces. Some porous structures formed by the network of the interlinked nanoparticles were observed from these TEM images. The average size of each NP was in the range of 50–60 nm. The material crystallinity was confirmed from the HR-TEM (Figure 5c) and SAED (Figure 5d) patterns, which depict that the prepared material is highly crystalline with a lattice distance of ~0.342 nm, and can be recognized to the (011) plane in inset IFFT reflection of the red circle. The SAED patterns showed that the fabricated material is polycrystalline and inconsistent with the XRD, complimenting the characterization and formation of the Ni-$CoWO_4$ nanoparticles.

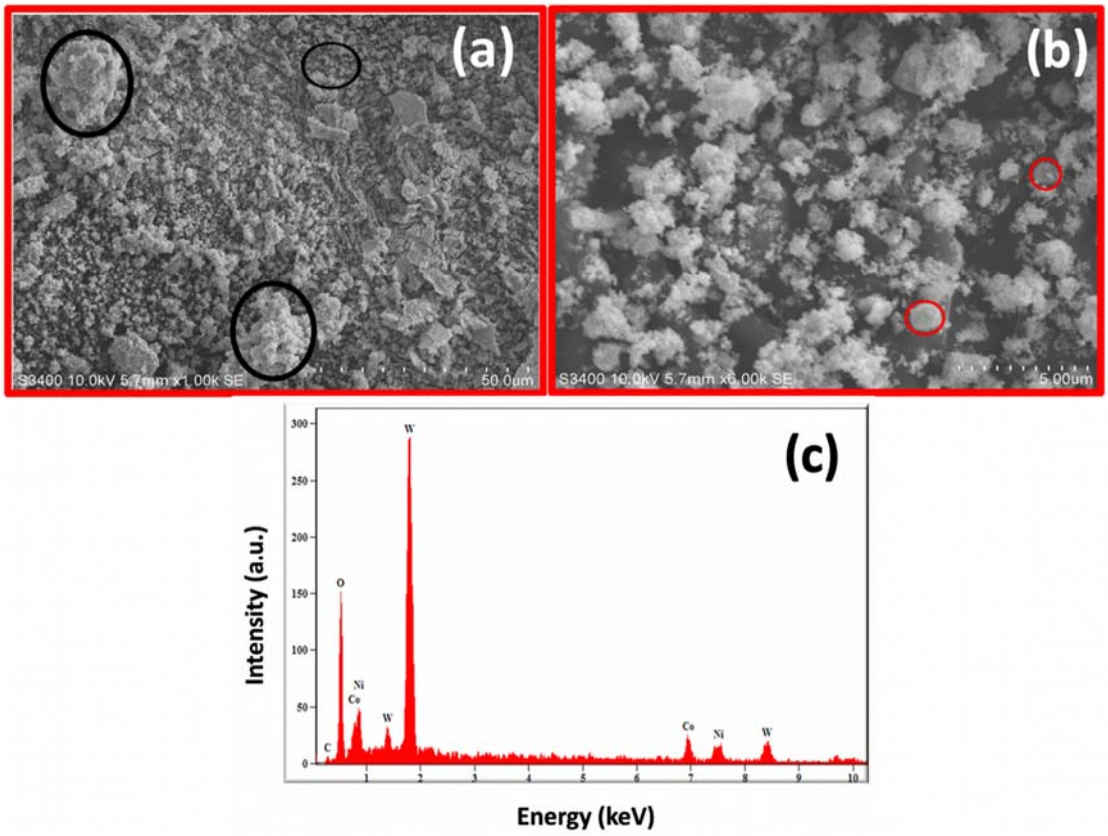

Figure 4. SEM images (**a**,**b**) with different magnification images and EDX spectrum (**c**) of Ni-$CoWO_4$ NPs.

3.5. BET Surface Area

The BET surface area for the calcined polycrystalline was conducted to evaluate their area, volume, and pore-size distribution. Figure 6 shows the nitrogen adsorption–desorption isotherm at 77 K and the corresponding pore-size distribution curves of the fabricated nanoparticles. The BET isotherm was recognized as type IV isotherm and H2-type hysteresis, confirming the mesoporous structures [40]. The surface area was found to be 20.19 m^2/g. The porosity of the NCW-NPs was determined from the desorption branch of the pore-size distribution curve (inset of Figure 6) and shows the sharp distribution in the mesoporous region. The average pore diameter and pore volume determined using the BJH method was found to be 2.22 nm and 0.075 cm^3/g, respectively. Based on the analysis, it may be assumed that the formed nanoparticles exhibit good porosity, which is one of the key factors for photocatalytic degradation.

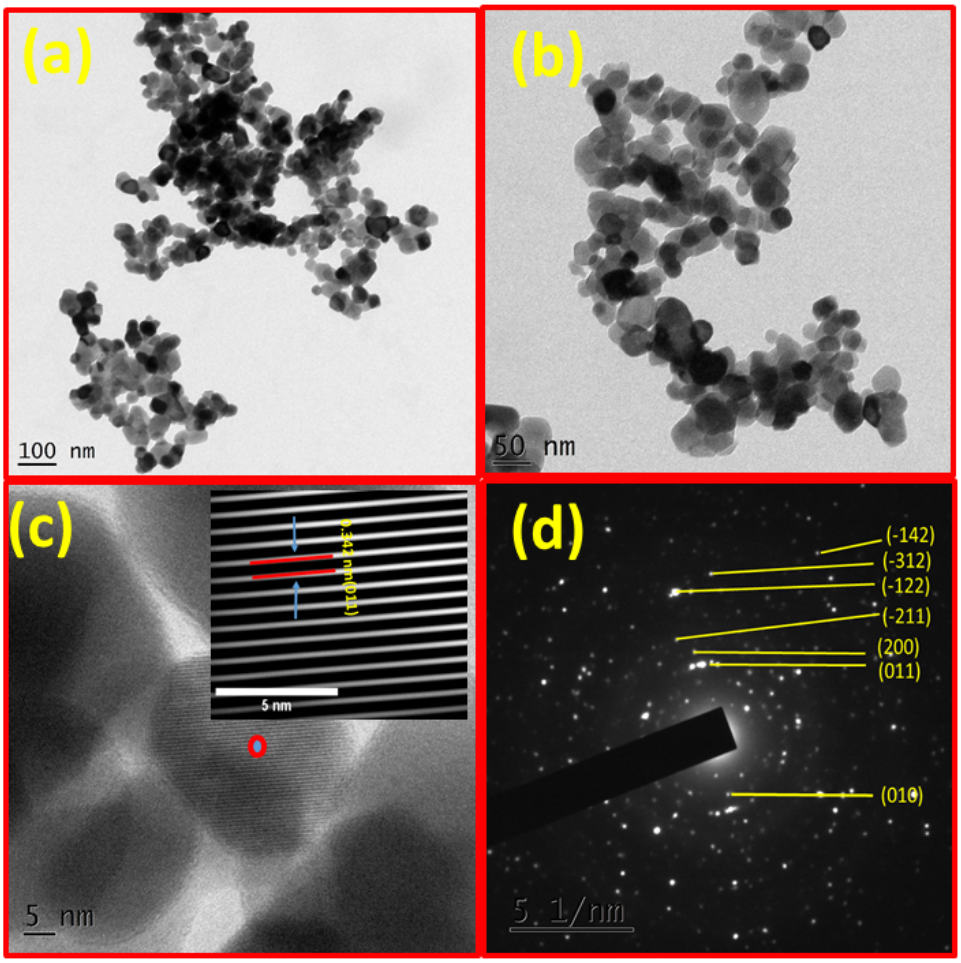

Figure 5. Shows the low (**a**) and high magnification (**b**) image of Ni-$CoWO_4$ NPs, (**c**) HR-TEM image and IFFT of the red circle (**d**) SAED diffraction patterns with *hkl* planes.

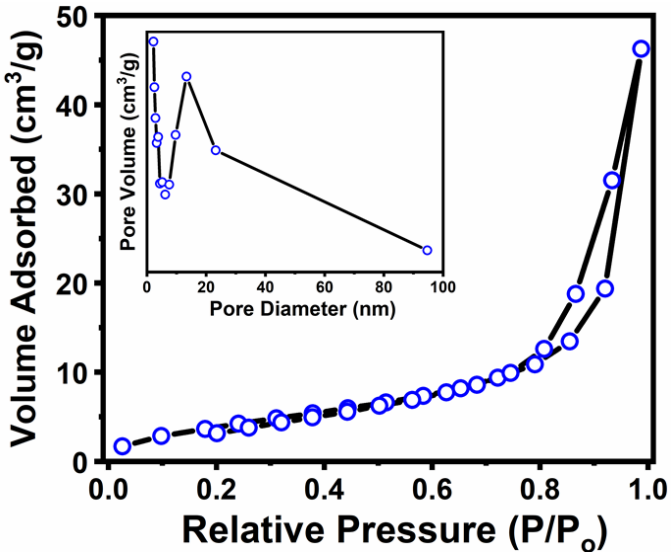

Figure 6. BET isotherms and inset corresponding to BJH pore-size distribution curves for the calcined Ni-$CoWO_4$ NPs.

3.6. Photocatalytic Evaluation

To evaluate the photocatalytic activities of the Ni-$CoWO_4$ nanoparticles, the photocatalytic decomposition of MB and RB under a 300 W Xe lamp with a 420 nm cutoff filter irradiation was selected as a model dye. Figure 7a,b shows the typical absorption spectra of the MB and RB aqueous solution (5 ppm) in the presence of the photocatalyst (50 mg) under visible-light illumination at ambient temperature and different time intervals. We observed that the intensity of the characteristic major absorption peaks of dyes (MB: 663 nm and RB: 547 nm) decreased as the exposure time extended. The peak intensity of RB (Figure 7b) decreased faster over time, about 80% degraded in 30 min and solutions became colorless after the required times. Hence, a decrease in the dye's concentration/absorption intensity indicated that the fabricated tungstate is a photoactive material toward RB. Moreover, the degradation efficiency of the dyes was evaluated using Equation (1) and is shown in Figure 7c. It was observed that RB was more degradable compared to MB in the presence of a catalyst. About 92.29% and 48.73% for RB and MB were mineralized, respectively, which demonstrated more photocatalytic degradation of RB due to interaction between the fabricated catalyst and anionic RB dye. Furthermore, the presence of a second Ni metal in Ni-$CoWO_4$, obtained by the hydrothermal approach, enhanced the surface area for the photocatalytic degradation. During the photocatalytic process, both transition metals exhibited variable oxidation states due to charge transfer and provide more accessibility of active sites in fabricated NCW-NPs. These results overcome the limitations of poor performance of monometallic tungstate, as previously reported [10–12,15,16].

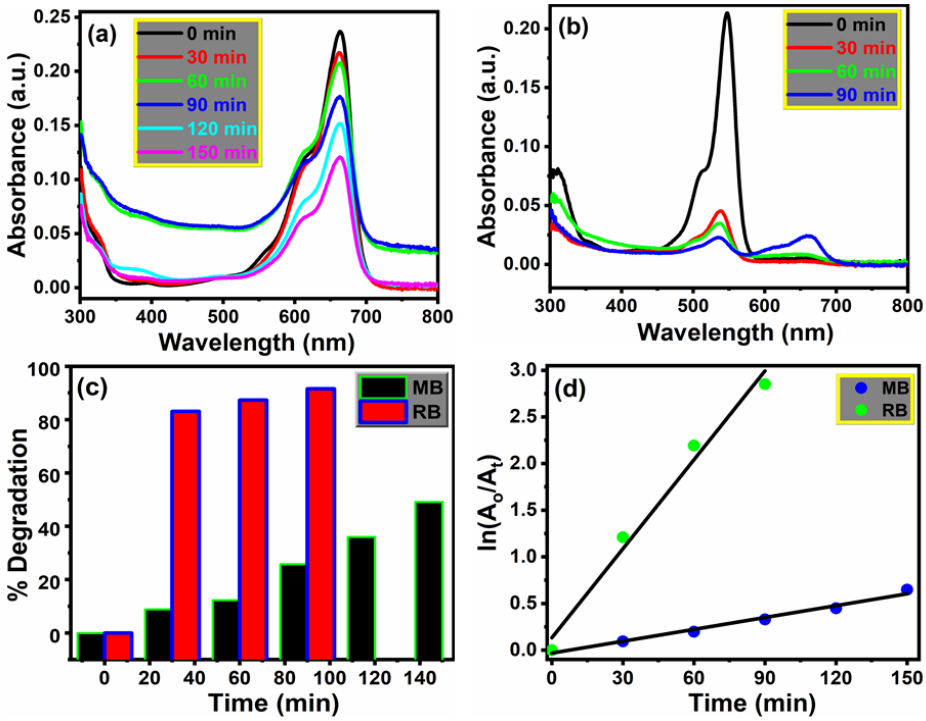

Figure 7. Absorption spectra of dyes at various time intervals under visible-light irradiation: (**a**) methylene blue, and (**b**) rose bengal dye. (**c**) Photocatalytic degradation of dyes and (**d**) kinetic relationship of $ln(A_o/A_t)$ vs. irradiation time.

From Figure 7d, we observed that the kinetics of the photocatalytic degradation of the dyes followed the Langmuir–Hinshelwood first-order kinetics model, which is described in the experimental section. The rate constants, by linear extrapolations, and half-life ($t_{1/2}$), were calculated and are summarized in Table 2. The rate constant value of the catalyst was better for RB compared with MB, which was around seven times (3.198×10^{-2} min^{-1}) higher than MB (0.437×10^{-2} min^{-1}).

Table 2. Kinetic parameters for Ni-$CoWO_4$ toward dyes MB and RB.

Dye	Degradation (%)	Rate Constant (min^{-1})	$t_{1/2}$(min)	R^2
MB	48.73	0.437×10^{-2}	158.45	0.977
RB	92.29	3.198×10^{-2}	21.72	0.975

The comparison of the degradation efficiency of our fabricated tungstate with the previously reported polyoxometalates is tabulated in Table 3 [18,41–46]. The present NCW-NPs showed comparable or higher photocatalytic degradation of MB, depending on the preparation and experimental conditions.

Table 3. Comparison of the photocatalytic activity of Ni-$CoWO_4$ with other tungstates.

Photocatalyst	Dye	Light Source	Time (min)	Degradation (%)	Ref.
Ni-$CoWO_4$	RB	300 W, Xe	90	92.28	TW
	MB	300 W, Xe	150	48.72	TW
$BaWO_4$	MB	250 W, Hg	120	21.06	18
$CuWO_4$	MB	500 W, Xe	80	78	41
$CoWO_4$	MB	Med. Pressure Hg	120	18.6	42
NiWO4	MB	Med. Pressure Hg	120	92.5	42
CuWO4	MB	Med. Pressure Hg	120	12.5	42
ZnWO4	MB	Med. Pressure Hg	120	2.72	42
ZnWO4	MB	Low Pressure Hg	60	>50	43
a-$SnWO_4$	MB	300 W, W	240	99	44
Bi_2WO_6	MB	50 W, Halogen	60	23	45
0.5$BiFeO_3$-0.5Bi_2WO_6	MB	50 W, Halogen	60	54	45
Fe_3O_4/$FeWO_4$	MB	500 W, Xe	60	97.1	46

To understand the photocatalysis mechanism of the NCW-NPs, the active species generated during the photocatalytic degradation were identified through radical and hole-trapping experiments. TBA, EDTA, AA, and $K_2Cr_2O_7$ acted as the scavengers for hydroxyl radicals ($^{\bullet}OH$), holes (h^+), superoxide radicals ($^{\bullet}O_2^-$), and electrons (e^-), respectively, and the obtained data in terms of degradation efficiency are represented in Figure 8a. From Figure 8a, it was observed that the degradation efficiency of RB without scavengers was 92.29%. However, the degradation efficiency of RB decreased slightly from 92.29% to 90.15% with the addition of EDTA, AA, and dichromate and considerable with the addition of TBA. This phenomenon suggests that hydroxyl radicals ($^{\bullet}OH$) played a major role in the degradation mechanism of RB, whereas other scavengers showed no effect.

To further the photocatalytic mechanism of the fabricated NPs by generating hydroxyl radicals, a photoluminescence probing technique was conducted with commonly used coumarin [47]. In this experiment, 5 mg of the photocatalyst was dispersed in 100 mL of 10^{-3} M (1 mM) coumarin solution. The solution was kept for adsorption–desorption equilibrium between the photocatalyst and coumarin before irradiation. This reaction was irradiated under visible light, for every 10 min, 2 mL of irradiated sample was withdrawn and the photoluminescence spectrum was measured. In the presence of the catalyst, non-luminescent coumarin reacted with ($^{\bullet}OH$) and was converted to highly fluorescent 7-hydroxyl coumarin on exposure to visible light. The photoluminescence spectra of NCW-NPs/coumarin solution under visible-light irradiation are displayed in Figure 8b, where the emission peak of coumarin (λ_{max} = 454 nm) increases continuously with irradiation

time. In this way, we can detect the formation of photo-generated (•OH) by monitoring the fluorescence intensity changes of the solution, concluding that the hydroxyl radical is a reactive species during the decomposition process.

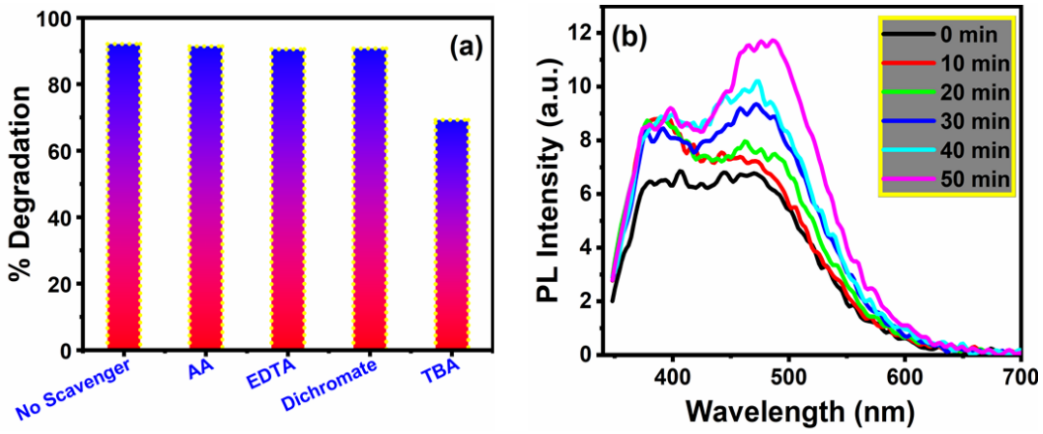

Figure 8. (**a**) Effects of different scavengers on degradation efficiency of RB and (**b**) photoluminescence spectrum against irradiation time.

Therefore, based on the findings of the active species, we can conclude that photocatalytic degradation begins with the generation of a (e^-–h^+) pairs. When a semiconductor photocatalyst is illuminated by light, with energy equal to or greater than the bandgap energy, the valence band (VB) electrons (reducing agent) can be excited to the conduction band, leaving a positive hole (oxidizing agent) in the valence band, as illustrated in Figure 9. Then, these photo-induced holes in VB of NCW-NPs react with the pollutant or H_2O/surface ^-OH, leading to the formation of hydroxyl radicals (•OH), which decompose RB to CO_2 and H_2O molecules. Therefore, a hydroxyl radical is recognized to be the most powerful oxidizing species in our case and can attack organic pollutants present at or near the surface of the photocatalyst.

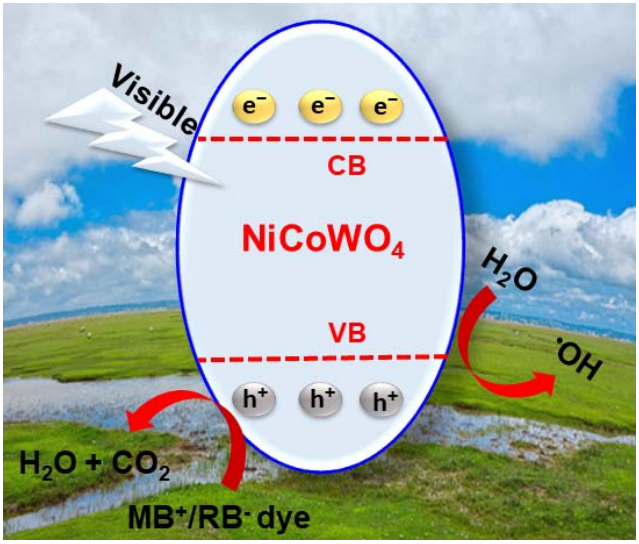

Figure 9. Schematic representation of dye degradation by calcined Ni-$CoWO_4$ NPs.

4. Conclusions

In this study, we reported on the hydrothermal synthesis of bimetallic Ni-$CoWO_4$ nanoparticles (NCW-NPs), and their formation was confirmed using XRD, IR, Raman, SEM-EDX, and HR-TEM. The fabricated nanoparticles showed better crystalline properties after calcination at 600 °C for 6 h. The morphology investigated by SEM revealed that

several nanoparticles combined in the form of spherical, smooth particles with an average diameter of a spherical cluster of 10–12 µm. Elemental analysis was conducted using EDX attached to the SEM, which showed a purity and relative percentage proportion of Ni, Co, W, and O in the NCW-NPs. Furthermore, its microstructure was confirmed via HR-TEM analysis, which showed that the average particle size of each NP was about 50 nm, well-arranged spherical and in a cubic shaped structure. The fringe distance between the two lattices was about 0.342 nm. The Raman peaks for the Ni–O, Co–O and W=O of the material were consistent with the HR-TEM and XRD. The obtained results from the characterization and photolytic activity test indicate that the fabricated NCW-NPs expressed better photocatalytic activity for RB compared to MB because of the synergistic effect and excellent redox ability of electron-hole pairs. As such, the processed materials can be used in large-scale industrial applications.

Author Contributions: F.A.A. and N.A played an important role in the project design and execution, while A.A.A. carried out the experimental work. H.S.A. and A.A.A. played a crucial role in the characterization and elucidation of the results. F.A.A. and N.A. compiled the data and prepared the manuscript. All authors have read and agreed to the published version of the manuscript.

Funding: This research received no external funding.

Institutional Review Board Statement: Not applicable.

Informed Consent Statement: Not applicable.

Acknowledgments: We thank the King Saud University, Deanship of Scientific Research for funding this work through the research group No. RG-1441-305. The authors thank the Deanship of Scientific Research and RSSU at King Saud University for their technical support.

Conflicts of Interest: The authors declare no conflict of interest.

References

1. Lopez, X.A.; Fuentes, A.F.; Zaragoza, M.M.; Guillén, J.A.D.; Gutiérrez, J.S.; Ortiz, A.L.; Martinez, V.C. Synthesis, characterization and photocatalytic evaluation of MWO_4 (M = Ni, Co, Cu and Mn) tungstates. *Int. J. Hydrog. Energy* **2016**, *41*, 23312–23317. [CrossRef]
2. Li, C.; Xu, Y.; Tu, W.; Chen, G.; Xuel, R. Metal-free photocatalysts for various applications in energy conversion and environmental purification. *Green Chem.* **2017**, *19*, 882. [CrossRef]
3. Sadiq, M.M.J.; Shenoy, U.S.; Bhat, D.K. High performance dual catalytic activity of novel zinc tungstate-reduced graphene oxide nanocomposites. *Adv. Sci. Eng. Med.* **2017**, *9*, 115–121.
4. Kumara, S.; Ojha, A.K. Ni, Co and Ni–Co co-doping induced modification in shape, optical band gap and enhanced photocatalytic activity of CeO_2 nanostructures for photodegradation of methylene blue dye under visible light irradiation. *RSC Adv.* **2016**, *6*, 8651. [CrossRef]
5. Qin, R.; Meng, F.; Khan, M.W.; Li, B.Y.H.; Fan, Z.; Gong, J. Fabrication and enhanced photocatalytic property of TiO_2-ZnO composite photocatalysts. *Mater. Lett.* **2019**, *240*, 84–87. [CrossRef]
6. Alharthi, F.A.; Al-Zaqri, N.; El-marghany, A.; Alghamdi, A.A.; Alorabi, A.Q.; Baghdadi, N.; Shehri, H.S.A.; Wahab, R.; Ahmad, N. Synthesis of nano cauliflower ZnO photocatalyst by potato waste and its photocatalytic efficiency against dye. *J. Mater. Sci. Mater. Electron.* **2020**, *31*, 11538. [CrossRef]
7. Alharthi, F.A.; Alghamdi, A.A.; Al-Zaqri1, N.; Alanazi, H.S.; Alsyahi, A.A.; El Marghany, A.; Ahmad, N. Facile one-pot green synthesis of Ag–ZnO Nanocomposites using potato peel and their Ag concentration dependent photocatalytic properties. *Sci. Rep.* **2020**, *10*, 20229. [CrossRef] [PubMed]
8. Alharthi, F.A.; Alghamdi, A.A.; Alanazi, H.S.; Alsyahi, A.A.; Ahmad, N. Photocatalytic Degradation of the Light Sensitive Organic Dyes: Methylene Blue and Rose Bengal by Using Urea Derived g-C_3N_4/ZnO Nanocomposites. *Catalysts* **2020**, *10*, 1457. [CrossRef]
9. Alharthi, F.A.; Alghamdi, A.A.; Alothman, A.A.; Almarhoon, Z.M.; Alsulaiman, M.F.; Al-Zaqri, N. Green Synthesis of ZnO Nanostructures Using Salvadora Persica Leaf Extract: Applications for Photocatalytic Degradation of Methylene Blue Dye. *Crystals* **2020**, *10*, 441. [CrossRef]
10. Esparza, P.; Hernández, T.; Borges, M.E.; Álvarez-Galván, M.C.; Ruiz-Morales, J.C.; Fierro, J.L.G. TiO_2 modifications by hydrothermal treatment and doping to improve its photocatalytic behaviour under visible light. *Catal. Today* **2013**, *210*, 135–141. [CrossRef]
11. Ma, D.; Xin, Y.; Gao, M.; Wu, J. Fabrication and photocatalytic properties of cationic and anionic S-doped TiO_2 nanofibers by electrospinning. *Appl. Catal. B Environ.* **2014**, *147*, 49–57. [CrossRef]

12. Choi, W.Y.; Termin, A.; Hoffmann, M.R. The Role of Metal Ion Dopants in Quantum-Sized TiO_2: Correlation between Photoreactivity and Charge Carrier Recombination Dynamics. *J. Phys. Chem.* **1994**, *98*, 13669–13679. [CrossRef]
13. Meng, F.; Song, X.; Sun, Z. Photocatalytic activity of TiO_2 thin films deposited by RF magnetron sputtering. *Vacuum* **2009**, *83*, 1147–1151. [CrossRef]
14. Thuong, H.T.T.; Kim, C.T.T.; Quang, L.N.; Kosslick, H. Highly active brookite TiO_2-assisted photocatalytic degradation of dyes under the simulated solar−UVA radiation. *Prog. Nat. Sci. Mater. Int.* **2019**, *29*, 641–647. [CrossRef]
15. Chowdhury, A.P.; Shambharkar, B.H. Fabrication and characterization of BiOBr-$SnWO_4$ heterojunction nanocomposites with boosted photodegradation capability. *Chem. Eng. J. Adv.* **2020**, *4*, 100040. [CrossRef]
16. Yangjeh, A.H.; Gohari, M.S. Novel magnetic Fe_3O_4/ZnO/$NiWO_4$ nanocomposites: Enhanced visible-light photocatalytic performance through p-n heterojunctions. *Sep. Purif. Technol.* **2017**, *184*, 334–346. [CrossRef]
17. Sadiq, M.M.J.; Shenoy, U.S.; Bhat, D.K. Synthesis of $BaWO_4$/NRGO–g-C_3N_4 nanocomposites with excellent multifunctional catalytic performance via microwave approach. *Front. Mater. Sci.* **2018**, *12*, 247–263. [CrossRef]
18. Rajpurohit, A.S.; Punde, N.S.; Rawool, C.R.; Srivastava, A.K. Fabrication of high energy density symmetric supercapacitor based on cobalt-nickel bimetallic tungstate nanoparticles decorated phosphorus-sulphur co-doped graphene nanosheets with extended voltage. *Chem. Eng. J.* **2019**, *371*, 679–692. [CrossRef]
19. Huang, H.; Liu, L.; Tian, N.; Zhang, Y. Structure, optical properties, and magnetism of $Zn_{1-x}Ni_xWO_4$ ($0 \leq x \leq 1$) solid solution. *J. Alloys Compd.* **2015**, *637*, 471–475. [CrossRef]
20. Zhang, M.C.; Fan, H.Q.; Zhao, N.; Peng, H.; Ren, X.H.; Wang, W.J.; Li, H.; Chen, G.Y.; Zhu, Y.N.; Jiang, X.B.; et al. 3D hierarchical $CoWO_4$/Co_3O_4 nanocone arrays for asymmetric supercapacitors with high energy density. *Chem. Eng. J.* **2018**, *347*, 291–300. [CrossRef]
21. Xu, X.; Yang, Y.; Wang, M.; Pei, D.; Robert, B.; Shen, J.F.; Ye, M.X. Straight forward synthesis of hierarchical Co_3O_4@$CoWO_4$/rGO core-shell arrays on Ni as hybrid electrodes for asymmetric supercapacitors. *Ceram. Int.* **2016**, *42*, 10719–10725. [CrossRef]
22. Sadiq, M.M.J.; Shenoy, U.S.; Bhat, D.K. $NiWO_4$–ZnO–NRGO ternary nanocomposite as an efficient photocatalyst for degradation of methylene blue and reduction of 4-nitrophenol. *J. Phys. Chem. Solids* **2017**, *109*, 124–133. [CrossRef]
23. Ai, Z.H.; Zhang, L.Z.; Lee, S.C.; Ho, W.K. Interfacial hydrothermal synthesis of Cu@Cu_2O core-shell microspheres with enhanced visible-light-driven photo-catalytic activity. *J. Phys. Chem. C* **2009**, *113*, 20896–20902. [CrossRef]
24. Zhang, M.; Fan, H.; Ren, X.; Zhao, N.; Peng, H.; Wang, C.; Wu, X.; Dong, G.; Long, C.; Wang, W.; et al. Study of pseudocapacitive contribution to superior energy storage of 3D heterostructure $CoWO_4$/Co_3O_4 nanocone arrays. *J. Power Sources* **2019**, *418*, 202–210. [CrossRef]
25. Xu, X.; Gao, J.; Huang, G.; Qiu, H.; Wanga, Z.; Wu, J.; Pan, Z.; Xing, F. Fabrication of $CoWO_4$@$NiWO_4$ nanocomposites with good supercapacitve performances. *Electrochim. Acta* **2015**, *174*, 837–845. [CrossRef]
26. Fan, M.S.; Zuhairi, A.A.; Bhatia, S. Utilization of greenhouse gases through dry reforming: Screening of nickel-based bimetallic catalysts and kinetic studies. *Chem. Sus. Chem.* **2011**, *4*, 643–653. [CrossRef]
27. Nathan, T.; Aziz, A.; Noor, A.F.; Prabaharan, S.R.S. Nanostructured NiO for electrochemical capacitors: Synthesis and electrochemical properties. *J. Solid State Electrochem.* **2008**, *12*, 1003–1009. [CrossRef]
28. Hotovy, I.; Huran, J.; Spiess, L.; Hascik, S.; Rehacek, V. Preparation of nickel oxide thin films for gas sensors applications. *Sens. Actuators B* **1999**, *57*, 147. [CrossRef]
29. Hosny, N.M. Synthesis, characterization and optical band gap of NiO nanoparticles derivedfrom anthranilic acid precursors via a thermal decomposition route. *Polyhedron* **2011**, *30*, 470–476. [CrossRef]
30. Yang, H.; Tao, Q.; Zhang, X.; Tang, A.; Ouyang, J. Solid-state synthesis and electrochemical property of SnO_2/NiO nanomaterials. *J. Alloy. Compd.* **2008**, *459*, 98. [CrossRef]
31. He, G.; Li, J.; Li, W.; Li, B.; Noor, N.; Xu, K.; Hu, J.; Parkin, I.P. One pot synthesis of nickel foam supported self-assembly of $NiWO_4$ and $CoWO_4$ nanostructures that act as high performance electrochemical capacitor electrodes. *J. Mater. Chem. A* **2015**, *3*, 14272–14278. [CrossRef]
32. Holzwarth, U.; Gibson, N. The Scherrer equation versus the 'Debye-Scherrer equation'. *Nat. Nanotechnol.* **2011**, *6*, 534. [CrossRef] [PubMed]
33. Xu, X.; Pei, L.; Yang, Y.; Shen, J.; Ye, M. Facile synthesis of $NiWO_4$/reduced graphene oxide nanocomposite with excellent capacitive performance for supercapacitors. *J. Alloy. Compd.* **2016**, *654*, 23–31. [CrossRef]
34. Appavu, B.; Kannan, K.; Thiripuranthagan, S. Enhanced visible light photocatalytic activities of template free mesoporous nitrogen doped reduced graphene oxide/titania composite catalysts. *J. Ind. Eng. Chem.* **2016**, *36*, 184–193. [CrossRef]
35. Xu, X.; Shen, J.; Li, N.; Ye, M. Facile synthesis of reduced graphene oxide $CoWO_4$ nanocomposites with enhanced electrochemical performances for supercapacitors. *Electrochim. Acta* **2014**, *150*, 23–34. [CrossRef]
36. Niu, L.; Li, Z.; Xu, Y.; Sun, J. Simple synthesis of amorphous $NiWO_4$ nanostructure and its application as a novel cathode material for asymmetric supercapacitors. *ACS Appl. Mater. Interfaces* **2013**, *5*, 8044–8052. [CrossRef] [PubMed]
37. Fonzo, F.D.; Bailini, A.; Russo, V.; Baserga, A.; Cattaneo, D.; Beghi, M.G.; Ossi, P.M.; Casari, C.S.; Bassi, A.L.; Bottani, C.E. Synthesis and characterization of tungsten and tungsten oxide nanostructured films. *Catal. Today* **2006**, *116*, 69–73. [CrossRef]
38. Ram, J.; Singh, R.G.; Gupta, R.; Kumar, V.; Singh, F.; Kumar, R. Effect of Annealing on the Surface Morphology, Optical and and Structural Properties of Nanodimensional Tungsten Oxide Prepared by Coprecipitation Technique. *J. Electron. Mater.* **2019**, *48*, 1174–1183. [CrossRef]

39. Kolesov, B. Raman investigation of H_2O molecule and hydroxyl groups in the channels of hemimorphite. *Am. Mineral.* **2006**, *91*, 1355–1362. [CrossRef]
40. Gregg, S.J.; Sing, K.S.W. *Adsorption, Surface Area, and Porosity*, 2nd ed.; Academic Press: London, UK, 1983.
41. Liang, L.; Liu, H.; Xie, X. Fabrication of novel $CuWO_4$ hollow microsphere photocatalyst for dye degradation under visible-light irradiation. *Mater. Lett.* **2016**, *182*, 302–304. [CrossRef]
42. Montini, T.; Gombac, V.; Hameed, A.; Felisari, L.; Adami, G.; Fornasiero, P. Synthesis, characterization and photocatalytic performance of transition metal tungstates. *Chem. Phys. Lett.* **2010**, *498*, 113–119. [CrossRef]
43. Garadkar, K.M.; Ghule, L.A.; Sapnar, K.B.; Dhole, S.D. A facile synthesis of $ZnWO_4$ nanoparticles by microwave assisted technique and its application in photocatalysis. *Mater. Res. Bull.* **2013**, *48*, 1105–1109. [CrossRef]
44. Alharthi, F.A.; Shashank, M.; Shashikanth, J.; Viswantha, R.; Alghamdi, A.A.; Algethami, J.; Alsaiari, M.A.; Jalalah, M.S.; Ganganagappa, N. Hydrothermal synthesis of α-$SnWO_4$: Application to lithium-ion battery and photocatalytic activity. *Ceram. Int.* **2021**, in press. [CrossRef]
45. Chaiwichian, S.; Wetchakun, K.; Kangwansupamonkon, W.; Wetchakun, N. Novel visible-light-driven $BiFeO_3$-Bi_2WO_6 nanocomposites toward degradation of dyes. *J. Photochem. Photobiol. A Chem.* **2017**, *349*, 183–192. [CrossRef]
46. Cao, X.; Chen, Y.; Jiao, S.; Fang, Z.; Xu, M.; Liu, X.; Li, L.; Pang, G.; Feng, S. Magnetic photocatalysts with a p–n junction: Fe_3O_4 nanoparticle and $FeWO_4$ nanowire heterostructures. *Nanoscale* **2014**, *6*, 12366–12370. [CrossRef] [PubMed]
47. Barreto, J.C.; Smith, G.S.; Strobel, N.H.P.; McQuillin, P.A.; Miller, T.A. Terephthalic acid: A dosimeter for the detection of hydroxyl radicals in vitro. *Life Sci.* **1995**, *56*, 89. [CrossRef]